Evidence for Dissociation and Ionization in Shock Compressed Nitrogen to 800 GPa

Yong-Jae Kim,[1,*] Burkhard Militzer,[2] Brian Boates,[1] Stanimir Bonev,[1] Peter M. Celliers,[1] Gilbert W. Collins,[3] Kevin P. Driver,[1] Dayne E. Fratanduono,[1] Sebastien Hamel,[1] Raymond Jeanloz,[2] J. Ryan Rygg,[3] Damian C. Swift,[1] Jon H. Eggert,[1] and Marius Millot[1,†]

[1]*Lawrence Livermore National Laboratory, Livermore, California 94550, USA*

[2]*Departments of Earth and Planetary Science and Astronomy, University of California, Berkeley, California 94720, USA*

[3]*Departments of Mechanical Engineering, Physics and Astronomy, and the Laboratory for Laser Energetics, University of Rochester, Rochester, New York 14623, USA*

(Received 24 November 2021; accepted 12 May 2022; published 27 June 2022)

Triple bonding in the nitrogen molecule (N_2) is among the strongest chemical bonds with a dissociation enthalpy of 9.8 eV/molecule. Nitrogen is therefore an excellent test bed for theoretical and numerical methods aimed at understanding how bonding evolves under the influence of the extreme pressures and temperatures of the warm dense matter regime. Here, we report laser-driven shock experiments on fluid molecular nitrogen up to 800 GPa and 4.0 g/cm^3. Line-imaging velocimetry measurements and impedance matching method with a quartz reference yield shock equation of state data of initially precompressed nitrogen. Comparison with numerical simulations using path integral Monte Carlo and density functional theory molecular dynamics reveals clear signatures of chemical dissociation and the onset of L-shell ionization. Combining data along multiple shock Hugoniot curves starting from densities between 0.76 and 1.29 g/cm^3, our study documents how pressure and density affect these changes in chemical bonding and provides benchmarks for future theoretical developments in this regime, with applications for planetary interior modeling, high energy density science, and inertial confinement fusion research.

DOI: 10.1103/PhysRevLett.129.015701

Elemental nitrogen ($Z = 7$) forms diatomic N_2 molecules with extremely strong triple covalent bonds (9.8 eV/molecule) at 300 K and 1 bar. This unique bonding yields not only stability and chemical inertia, but also a diverse solid-state polymorphism over a wide range of pressure-temperature conditions. The gradual evolution of chemical bonding and molecular or atomic rearrangements under elevated pressure and temperature are of great interest, as nitrogen is expected to be present in icy planet interiors [1,2], is also an important detonation product [3,4], and is critical to many energetic materials [5]. For example, static compression studies of this simple molecular system using diamond anvil cells at low and moderate temperature have revealed more than 15 solid phases differing by subtle rearrangements of the nitrogen molecules driven by pressure-induced symmetric breaking [6–8], or the weakening and breaking of the triple bonds to form single-bonded polymeric phases [9–11].

Upon increasing temperature well above 1000 K, molecular fluid nitrogen has been predicted to transform into an atomic fluid, a polymeric fluid, and a strongly coupled plasma [12–16]. Therefore, this prototypical low-Z molecular system is an excellent test bed for the development of advanced numerical and theoretical approaches for matter in the high energy density regime [17] and inertial confinement fusion science [18]. For example, recent experiments have shown that the shock density of deuterium (D_2) near 400–1000 GPa along a double shock path, starting from the cryogenic liquid, cannot be reconciled with predictions from density functional theory molecular dynamics (DFTMD) and broad-range equation of state (EOS) models [19]. Having a heavier atomic nucleus, nitrogen's properties may be easier to capture with current quantum simulation techniques. We expect a negligible quantum zero-point motion, a reliable Born-Oppenheimer approximation, and an accurate classical description of ion dynamics in DFTMD for nitrogen at high pressure and temperature conditions [15]. Studying nitrogen might therefore help to unlock some of the mysteries regarding the behavior of hydrogen in the warm dense regime—with important implications for inertial confinement fusion science—by providing a means to compare theoretical and numerical approaches with experimental data for bonding changes and ionization of a low-Z diatomic molecule in the absence of the key complexities that arise when dealing with H atoms.

While various other low-Z materials have been studied under extreme conditions using dynamic compression experiments [17,20–23], there are few experimental results to compare with simulations for nitrogen above 100 GPa [24,25]. Most shock compression experiments on molecular nitrogen have been performed on the cryogenic fluid with initial density ρ_{LN} of 0.81 g/cm^3 (at 77 K) with planar

impactors [25–32] up to 80 GPa. These revealed the onset of molecular dissociation into an atomic fluid at 30 GPa and 2.3-fold compression by comparing with a theoretical molecular Hugoniot [30,33], and evidence of its completion at 80 GPa and 3.7-fold compression [30,32] in agreement with DFTMD simulations [15]. The only available shock EOS data in the multimegabar regime, obtained with hemispherical-shell impacts, reported an isochoric compression at 4.2-fold compression between 100 and 320 GPa. This was interpreted as evidence for a polymeric fluid state [24,25] and supported by average-atom simulations [14], but appears to be in stark disagreement with the DFTMD simulations.

In this study, we performed laser-driven shock experiments on fluid molecular nitrogen precompressed in diamond and sapphire anvil cells to provide new experimental data in the range of this discrepancy between experiments and quantum simulations. Doppler velocimetry and impedance matching with a quartz reference were used to document the shock pressure-density EOS of nitrogen up to 800 GPa, 2.5 times higher pressure than those of previous studies [24]. The behavior observed in our new data is well captured by DFTMD simulations, and reveals clear signatures of the chemical dissociation of molecular nitrogen into an atomic fluid and the onset of L-shell ionization across a wide range of pressure-density-temperature conditions.

The precompressed laser-shock targets were prepared using diamond and sapphire anvil cells [see Fig. 1(a) and Supplemental Material [34]]. Liquid nitrogen was loaded cryogenically into the high-pressure cell, then compressed at room temperature to an initial pressure (P_0) of 0.23–2.03 GPa, measured by ruby luminescence [45]. The density (ρ_0) and refractive index (n_0) of the preshot sample were inferred as 0.76–1.29 g/cm^3 and 1.18–1.32, respectively, based on previous studies [46–50], and are listed in Table S1 [34].

We conducted 21 shock experiments on the Omega Laser Facility at the University of Rochester (New York). We used up to 12 beams with 23° or 48° incident angles to deliver 0.7–6.0 kJ of 351 nm UV laser in a 1 ns super-Gaussian flattop pulse with a ~0.1 ns 10%–90% rise time. Phase plates (SG8 with a 438 μm radius at e^{-1} maximum intensity and a 4.5 super-Gaussian exponent, and E-SG-865 with 430 and 396 μm major and minor radii and a 4.7 super-Gaussian exponent) were used to produce a flattop laser intensity distribution matching the 900 μm diameter opening on the drive side of the diamond anvil.

In the experiments described here, the initially transparent quartz and nitrogen become optically reflective under shock compression, so that the shock front can be directly tracked with a line-imaging velocity interferometer system for any reflector (VISAR). We record two VISAR channels (A and B) with 18.23 and 7.212 mm thick etalons, giving a vacuum velocity per fringe (VPF) of 2.732 and

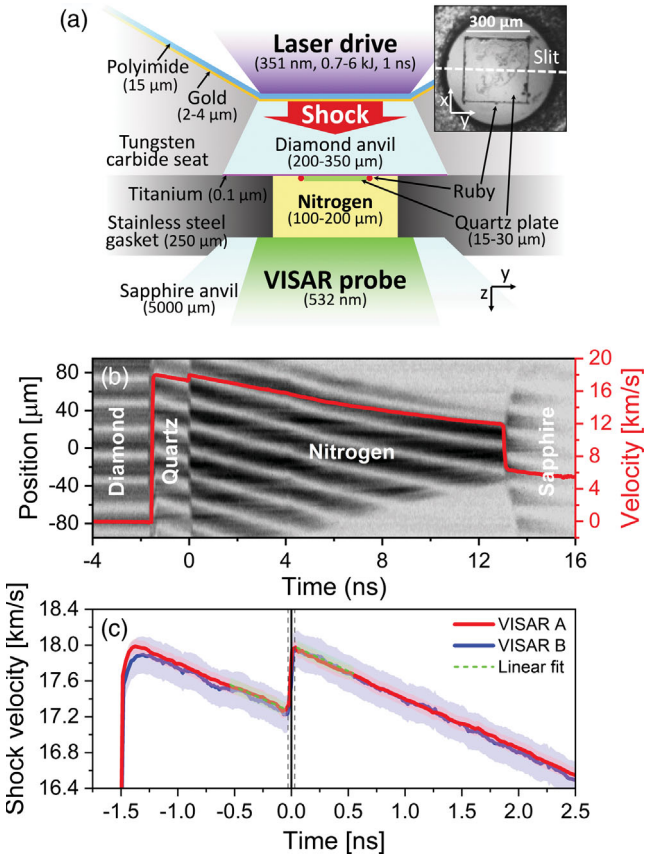

FIG. 1. (a) Sketch of the experimental configuration including the diamond and sapphire anvil cell target, the focus locations of the laser-drive beams, and Doppler velocimetry (VISAR) probe. Inset micrograph shows the pressure chamber containing transparent molecular nitrogen fluid, a quartz reference plate, and ruby pressure markers. The white dashed line represents the projection of the VISAR streak camera entrance slit onto the target. (b) Raw image for shot 65143, overlaid with the corresponding shock-front velocity history (red). (c) Velocity profiles for shot 65143 measured with the two VISAR channels (A and B), and the linear fitting and extrapolation of the higher-resolution velocity channel to the impedance match event (set as $t_{\mathrm{IM}} = 0$ s, black vertical line). Shaded area represents the systematic uncertainty for each channel. Black dotted vertical lines indicate the timing uncertainty for this event.

6.906 km/s/fringe: with distinct values of VPF, the two VISAR records allow us to confirm the magnitudes of fringe offsets at each interface. In Fig. 1(b), the shock wave arrives at the diamond-quartz interface (~ -2 ns), breaks out of the quartz into the sample ($t_{\mathrm{IM}} = 0$ ns), and transits through the nitrogen layer before entering the sapphire anvil (~18.5 ns). The stationary VISAR signal before −2 ns originates from the laser probe reflecting off the Ti mirror coating on the diamond.

Standard phase unwrapping and correction using the refractive indices $n_0(P_0)$ of the precompressed quartz and nitrogen yield the shock-front velocity history $U_S(t)$ shown in Figs. 1(b) and 1(c): $U_S = U_{\mathrm{app}}/n_0$, where U_{app} is the

apparent shock velocity [22,51,52]. We determine the shock velocities of the quartz ($U_{S,Q}$) and nitrogen sample (U_S) at their interface (t_{IM}) using the VISAR signal with the highest precision (i.e., VISAR A), by linearly fitting the velocity over 0.5–1.0 ns and extrapolating the fits to t_{IM}, as shown in Fig. 1(c). For each shot, we estimate the uncertainty of the phase retrieval by determining the value needed to get the error bars of the velocity traces from the two VISAR channels to overlap, which is found as 3%–5% of the VPF. From the jump in shock velocity between the incident shock in quartz and the transmitted shock in nitrogen, we determine how compressible nitrogen is relative to quartz with the impedance matching technique (see Supplemental Material [34] and related Refs. [53–55]). The measured shock velocities of quartz and nitrogen ($U_{S,Q}$ and U_S) and inferred shock states of nitrogen (u_p, P, ρ, and ρ/ρ_0) for each shot are summarized in Table S2 [34]. Error propagation including random and systematic errors is carried out using a Monte Carlo methodology with the Cholesky decomposition to generate correlated random variables from the covariance matrices of the various model parameters [22,34].

In order to compare with our experiments, shock Hugoniot curves are computed for five different initial densities including the cryogenic liquid density (0.81 g/cm^3), 0.91, 1.08, 1.16, and 1.27 g/cm^3 from the first-principles equation of state described in Refs. [15,56]. Depending on the temperature, these simulations use either DFTMD with the Perdew-Burke-Ernzerhof exchange-correlation functional in the generalized gradient approximation or path integral Monte Carlo (PIMC) methods. We computed the change in internal energy induced by the precompression, then solved the energy conservation Rankine-Hugoniot equation for specific internal energy, using a bicubic spline in density-temperature space. Along the Hugoniot curves considered here, the switch from DFTMD to PIMC occurs around 3000 GPa. We note that the difference in internal energy between the cryogenic and precompressed fluids at 0.81 g/cm^3 (~0.06 eV/molecule) is much smaller than the shock-induced internal energy variation (~5–100 eV/molecule); see Figs. S2 and S1 [34].

The U_S versus u_p data for our 21 experiments on precompressed nitrogen are plotted in Fig. 2(a) and compared with the results of previous experimental studies on cryogenic liquid nitrogen [24–29,32], including the gas-gun study up to 80 GPa by Nellis *et al.* [32] (square) and the hemi-spherical explosive experiments up to 320 GPa by Trunin *et al.* [24] and Mochalov *et al.* [25] (pentagon and star); for their initial conditions, see Table S3 [34]. We also plot a series of simulated Hugoniot curves with various ρ_0 (with density as a color scale). Our dataset extends over a broad range of U_S, from 10.3 to 35.5 km/s, which is 1.5 times higher than previous results [24]. On such an extended scale, all data points appear to lie broadly scattered around a single line regardless of the ρ_0.

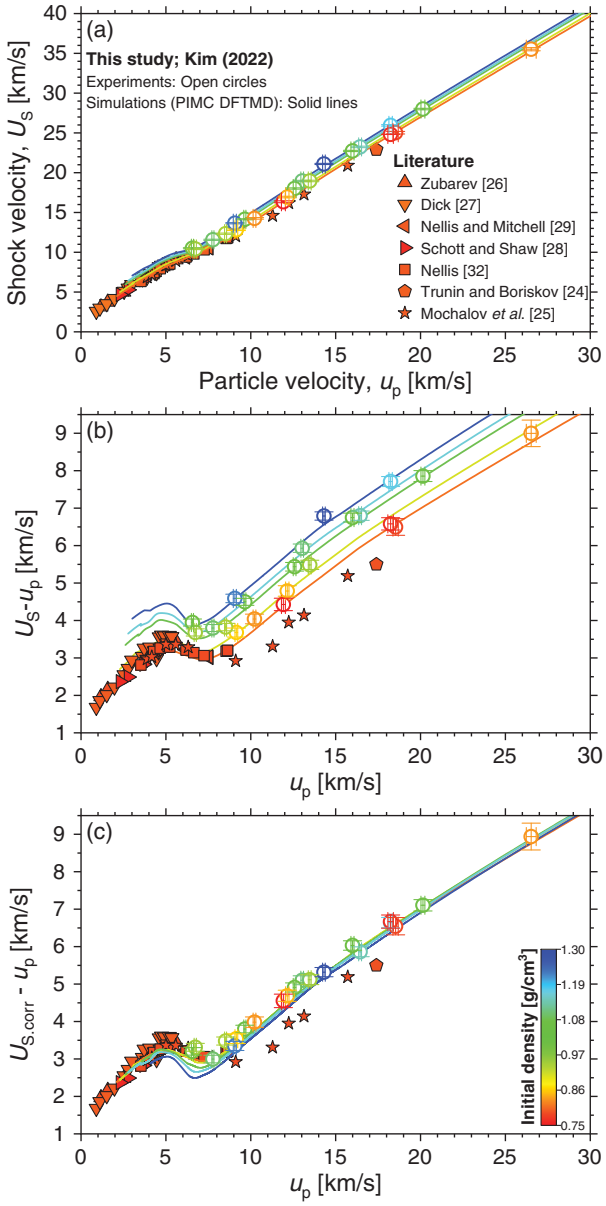

FIG. 2. Shock velocity versus particle velocity of nitrogen. (a) Our data extend the previously explored range [24–30]. (b) Showing the data in the U_S-u_p versus u_p plane reveals nonlinearity and initial density trends. (c) Shock velocities for various initial densities are corrected to match those for liquid nitrogen density, further enhancing the evidence for subtle changes in shock compression, and providing a basis for detailed comparison with the corresponding Hugoniot curves derived from PIMC DFTMD simulations [solid curves in (a)–(c)]. Color scale corresponds to the initial density of the nitrogen sample.

Plotting $U_S - u_p$ as a function of u_p on Fig. 2(b) helps to visualize nonlinearity and initial density trends better [57]. In this plot, our lowest velocity data appear to overlap with the bulk of the data points from previous studies on cryogenic liquid nitrogen. In addition, U_S clearly scales with ρ_0 as observed previously in D_2 [53], He [58], CO_2 [23], SiO_2 [54], and porous metals [59]. Indeed, a shift in

U_S proportional to ρ_0 is found to collapse all experimental data into a single line, allowing us to compare directly Hugoniot data with various initial states [Fig. 2(c) herein and Fig. S3 [34]].

We found that the Hugoniot curves simulated with the PIMC DFTMD methods agree with current and previous experimental data over a wide velocity range, except for the data from Refs. [24,25], which will be discussed later [Fig. 2(b)]. Both experimental and simulated data show two abrupt slope changes (i.e., softening and stiffening) near $u_p = 5$ and 8 km/s (Fig. S4 [34]). These are interpreted as signatures of the compression changes associated with the onset and completion of the shock-induced dissociation of the nitrogen molecules [24,25,30,32]. When the simulated U_S are corrected to account for their ρ_0, they overlap well before ($u_p < 5$ km/s) and after (> 8 km/s) the chemical dissociation region [Fig. 2(c)]. The extensive velocity overlap in the experiments and simulations confirms that the compressibility of different ρ_0 data are similar, despite the fact that our data span different P-T-ρ conditions. In other words, the bonding changes appear as smooth, rather than sharp transitions. However, a closer look at the family of simulated Hugoniot curves in the dissociation regime ($5 < u_p < 8$ km/s) suggests that the transition becomes sharper with increasing ρ_0, i.e., at lower temperature, as illustrated by the predicted dissociation boundary [13,15] which becomes a first-order transition at lower temperature and higher pressure (Fig. S5 [34]).

The P-ρ values of our low-ρ_0 data ($\rho_0 = 0.76$–0.87 g/cm^3) are plotted in Fig. 3(a), along with previous experimental data and various simulation curves for cryogenic liquid nitrogen. Our data range is 101–798 GPa and 2.78–3.38 g/cm^3, with a maximum compression of 4.18-fold over the liquid nitrogen density. We find that pressure increases from 100 to 400 GPa almost isochorically near 2.8–3.0 g/cm^3, corresponding to $\rho/\rho_{LN} = 3.5$–3.7. Above 400 GPa, shocked nitrogen reaches higher compression with increasing P up to our maximum pressure level of 800 GPa.

The Hugoniot curves derived from the simulations reproduce the behavior observed in the experimental data over a wide P-ρ range (10–800 GPa and 1.5–3.4 g/cm^3), and capture the slope changes near 30, 80, and 400 GPa quite well [Fig. 3(a)]. The two slope changes at lower pressures (i.e., softening and stiffening) are interpreted as signatures of the onset and completion of the chemical dissociation [30,32], as discussed above for Fig. 2(b). Consistently, the stiff behavior in the 100–400 GPa range apparent in our experimental data suggests that molecular dissociation is largely completed by ~100 GPa. Our simulation shows a compression maximum beyond the pressure level experimentally explored in this study (> 800 GPa), corresponding to complete L-shell ionization at 4000 GPa, 3.5 g/cm^3, and 4.3-fold compression [15]. This suggests the increased compressibility observed above

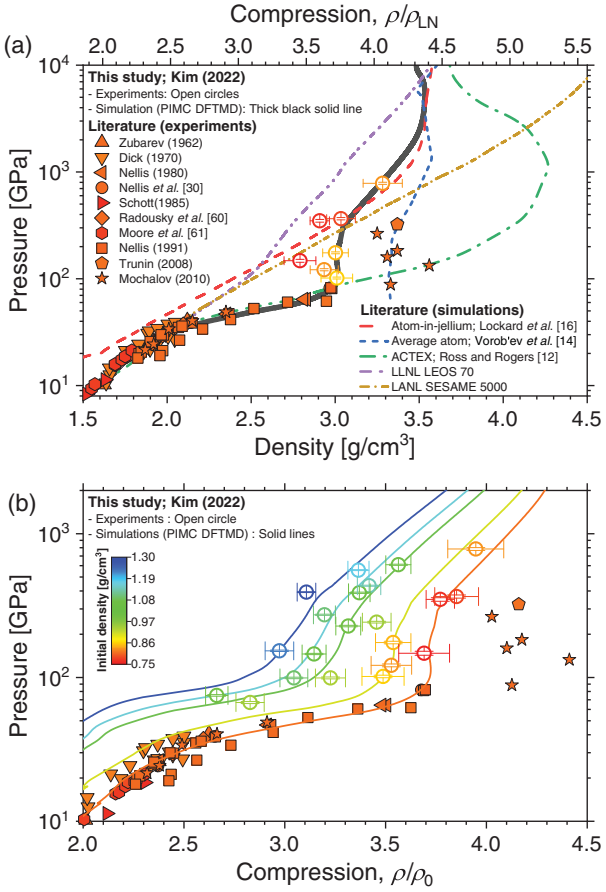

FIG. 3. Shock pressure versus density of nitrogen. (a) Comparison of experimental data in this ($\rho_0 = 0.76$–0.87 g/cm^3) and previous [24–30,32,60,61] studies with simulated Hugoniot curves using various models [12,14–16] for cryogenic liquid nitrogen. (b) Our experimental data for a wide range of initial densities ($\rho_0 = 0.76$–1.29 g/cm^3) are well described by the simulated Hugoniot curves. A common color scale representing the nitrogen sample's initial density is used for both experimental data and simulated Hugoniot curves.

400 GPa can be related to the onset of L-shell ionization of the dissociated atomic nitrogen.

We note that the previous data from hemispherical compressions [24,25] (pentagon and star) are slower [Fig. 2(b)] and denser [Fig. 3(a)] in the dissociated atomic regime, as compared with our experimental and simulation results. This discrepancy remains unexplained, but could arise from the neglect of 2D and possibly 3D effects in the analysis of those experiments which rely on hydrodynamic simulations to account for the shock's spherical convergence and acceleration. In addition, the reported uncertainty in the measured shock velocity in Ref. [25] ($\Delta U_S/U_S = 1.8\%$–3.3%) is much larger than in our experiments ($\Delta U_S/U_S = 0.1\%$–0.7%); for a further discussion, see Supplemental Material [34].

Our experimental and simulation results are also compared with predictions from various numerical and

theoretical methods in Fig. 3(a). First, the less computationally demanding atom-in-jellium approach [16] compares well with our data after the softening at 400 GPa. However, this model cannot capture chemical bonding, so it is inadequate in the molecular, dissociation, and atomic regimes. Next, the average-atom model [14] describes the isochoric compression and ionization-induced softening in a similar pressure regime as our results. However, as it reproduces the results by Trunin *et al.* [24] and Mochalov *et al.* [25] at higher density, this model is in disagreement with ours. The activity expansion (ACTEX) simulation curve [12] extrapolated below 2000 GPa to match the gas-gun data at 20–80 GPa is found to be inconsistent with our results. Finally, both the molecular vibration-based (SESAME 5000) and Thomas-Fermi (LEOS 70) models match experimental data very well below 30 GPa, but are inadequate above that shock pressure as they lack a description of the molecular dissociation and ionization phenomena. The SESAME 5000 approaches a maximum compression ratio of 6 (as expected for a perfect diatomic gas with the heat capacity ratio γ of 7/5 [62]), while the LEOS 70 exhibits a peak compression (not shown here) at a similar density but higher pressure than the L-shell ionization in the PIMC DFTMD simulations.

Our complete experimental P versus ρ/ρ_0 dataset ($\rho_0 = 0.76$–1.29 g/cm^3) is shown in Fig. 3(b). While the precompression allows us to reach denser shock states than the principal Hugoniot of cryogenic liquid nitrogen, and explore more extreme conditions of density for this material reaching 4.0 g/cm^3 (Fig. S8 [34]), we find that the shock compression ratio (ρ/ρ_0) is reduced with increasing precompression and initial density. This could be interpreted as being due to stronger particle interactions (which decrease the compression) at higher shock density and reduced excitation of internal degrees of freedom, such as molecular dissociation and thermal ionization (which increases the compression) for shock compression of an initially denser sample [15,58].

A closer look at our experimental data compared with the corresponding simulation curves [matching colors in Fig. 3(b)] provides further confidence in the ability of the DFTMD simulations to accurately capture the subtle changes in material properties at these previously undocumented conditions. Along the precompressed Hugoniot curves with $\rho_0 > 0.81$ g/cm^3, no stiff isochoric behavior is observed between 100 and 400 GPa. Rather, the compressibility in this pressure range increases gradually with ρ_0. This behavior is opposite to that expected for increased particle interactions, but implies that the excitation process becomes more important at lower pressures with increasing ρ_0. For a further understanding of nitrogen's behavior in the Mbar regime, we computed the electronic density of states with DFTMD simulations (Fig. S9 [34]) at various pressures (107–735 GPa) for a 3.706 g/cm^3 density (Figs. S5 and S8 [34]), showing that more L-shell electrons become excited above the Fermi energy with increasing pressure. This electronic excitation increases the internal energy, which leads to an increase in shock compression, as is discussed by Militzer [63]. Therefore, we reach the conclusion that the enhanced compression above 400 GPa, or 14 km/s in u_p [Fig. 2(c) herein and Fig. S6 [34]), can be understood as being due to L-shell ionization enhancing the compressibility of dissociated nitrogen.

Although the current experimental study with a kilojoule laser drive covers only the initiation of L-shell ionization at low pressures, recent measurements in spherical geometry [17] using a megajoule laser drive at the National Ignition Facility (NIF) clearly documented signatures of K-shell ionization of carbon in the 15–45 TPa range and could be used for future experiments on nitrogen. In addition, ongoing development of a new diamond anvil cell platform on NIF is paving the way to investigate equally interesting phenomena at much lower temperature such as the early observation of shock cooling [31] and the later prediction of a first-order transition between molecular fluid and polymeric fluid [15]. Altogether, the development of EOS measurement techniques opens novel opportunities to unravel matter's response to extreme conditions (e.g., dissociation, ionization, and electron degeneracy), enabling a better understanding of dense celestial objects such as white dwarfs and exoplanets.

This work was prepared by LLNL under Contract No. DE-AC52-07NA27344 and was supported by LLNL LDRD Program No. 19-ERD-031. Partial funding for G. W. C. and J. R. R. was provided by NSF Physics Frontier Center Grant No. PHY-2020249. We acknowledge technical assistance from Eric Folsom, Renee Posadas, Carol Davis, and Jim Emig. The data in this work were analyzed with LLNL AnalyzeVISAR code.

*kim100@llnl.gov
†millot1@llnl.gov

[1] W. B. Hubbard, Science **214**, 145 (1981).
[2] K. Soderlund, M. Bethkenhagen, I. de Pater, J. Fortney, S. Hamel, R. Helled, Y.-J. Kim, M. Millot, and S. Stanley, Bull. Am. Astron. Soc. **53**, 233 (2021).
[3] M. Bagge-Hansen *et al.*, Nat. Commun. **10**, 3819 (2019).
[4] M. C. Marshall, A. Fernandez-Pañella, T. W. Myers, J. H. Eggert, D. J. Erskine, S. Bastea, L. E. Fried, and L. D. Leininger, J. Appl. Phys. **127**, 185901 (2020).
[5] D. Badgujar, M. Talawar, S. Asthana, and P. Mahulikar, J. Hazard. Mater. **151**, 289 (2008).
[6] H. Katzke and P. Tolédano, Phys. Rev. B **78**, 064103 (2008).
[7] A. Erba, L. Maschio, C. Pisani, and S. Casassa, Phys. Rev. B **84**, 012101 (2011).
[8] R. Turnbull, M. Hanfland, J. Binns, M. Martinez-Canales, M. Frost, M. Marqués, R. T. Howie, and E. Gregoryanz, Nat. Commun. **9**, 4717 (2018).
[9] C. Mailhiot, L. H. Yang, and A. K. McMahan, Phys. Rev. B **46**, 14419 (1992).

[10] M. I. Eremets, A. G. Gavriliuk, I. a. Trojan, D. a. Dzivenko, and R. Boehler, Nat. Mater. **3**, 558 (2004).
[11] C. Ji, A. A. Adeleke, L. Yang, B. Wan, H. Gou, Y. Yao, B. Li, Y. Meng, J. S. Smith, V. B. Prakapenka, W. Liu, G. Shen, W. L. Mao, and H.-k. Mao, Sci. Adv. **6**, eaba9206 (2020).
[12] M. Ross and F. Rogers, Phys. Rev. B **74**, 024103 (2006).
[13] B. Boates and S. A. Bonev, Phys. Rev. Lett. **102**, 015701 (2009).
[14] V. S. Vorob'ev, A. S. Grushin, and V. G. Novikov, J. Chem. Phys. **137**, 031102 (2012).
[15] K. P. Driver and B. Militzer, Phys. Rev. B **93**, 064101 (2016).
[16] T. Lockard, M. Millot, B. Militzer, S. Hamel, L. X. Benedict, P. A. Sterne, and D. C. Swift, arXiv:1906.09516v2.
[17] A. L. Kritcher *et al.*, Nature (London) **584**, 51 (2020).
[18] S. Le Pape *et al.*, Phys. Rev. Lett. **120**, 245003 (2018).
[19] A. Fernandez-Pañella, M. Millot, D. E. Fratanduono, M. P. Desjarlais, S. Hamel, M. C. Marshall, D. J. Erskine, P. A. Sterne, S. Haan, T. R. Boehly, G. W. Collins, J. H. Eggert, and P. M. Celliers, Phys. Rev. Lett. **122**, 255702 (2019).
[20] P. M. Celliers *et al.*, Phys. Plasmas **11**, L41 (2004).
[21] P. Loubeyre, S. Brygoo, J. Eggert, P. M. Celliers, D. K. Spaulding, J. R. Rygg, T. R. Boehly, G. W. Collins, and R. Jeanloz, Phys. Rev. B **86**, 144115 (2012).
[22] M. Millot, S. Hamel, J. R. Rygg, P. M. Celliers, G. W. Collins, F. Coppari, D. E. Fratanduono, R. Jeanloz, D. C. Swift, and J. H. Eggert, Nat. Phys. **14**, 297 (2018).
[23] L. E. Crandall, J. R. Rygg, D. K. Spaulding, T. R. Boehly, S. Brygoo, P. M. Celliers, J. H. Eggert, D. E. Fratanduono, B. J. Henderson, M. F. Huff, R. Jeanloz, A. Lazicki, M. C. Marshall, D. N. Polsin, M. Zaghoo, M. Millot, and G. W. Collins, Phys. Rev. Lett. **125**, 165701 (2020).
[24] R. F. Trunin, G. V. Boriskov, A. I. Bykov, A. B. Medvedev, G. V. Simakov, and A. N. Shuikin, JETP Lett. **88**, 189 (2008).
[25] M. A. Mochalov, M. V. Zhernokletov, R. I. Il'kaev, A. L. Mikhailov, V. E. Fortov, V. K. Gryaznov, I. L. Iosilevskiy, A. B. Mezhevov, A. E. Kovalev, S. I. Kirshanov, Y. A. Grigor'eva, M. G. Novikov, and A. N. Shuikin, J. Exp. Theor. Phys. **110**, 67 (2010).
[26] V. N. Zubarev and G. S. Telegin, Dokl. Akad. Nauk SSSR **142**, 309 (1962), http://mi.mathnet.ru/dan26005.
[27] R. D. Dick, J. Chem. Phys. **52**, 6021 (1970).
[28] G. L. Schott, M. S. Shaw, and J. D. Johnson, J. Chem. Phys. **82**, 4264 (1985).
[29] W. J. Nellis and A. C. Mitchell, J. Chem. Phys. **73**, 6137 (1980).
[30] W. J. Nellis, N. C. Holmes, A. C. Mitchell, and M. van Thiel, Phys. Rev. Lett. **53**, 1661 (1984).
[31] H. B. Radousky and M. Ross, High Press. Res. **1**, 39 (1988).
[32] W. J. Nellis, H. B. Radousky, D. C. Hamilton, A. C. Mitchell, N. C. Holmes, K. B. Christianson, and M. van Thiel, J. Chem. Phys. **94**, 2244 (1991).
[33] M. Ross and F. H. Ree, J. Chem. Phys. **73**, 6146 (1980).
[34] See Supplemental Material at http://link.aps.org/supplemental/10.1103/PhysRevLett.129.015701 for more details, which includes Refs. [35–44].
[35] G. Ghosh, Opt. Commun. **163**, 95 (1999).
[36] E. Calderon, M. Gauthier, F. Decremps, G. Hamel, G. Syfosse, and A. Polian, J. Phys. Condens. Matter **19**, 436228 (2007).
[37] H. Kimizuka, S. Ogata, J. Li, and Y. Shibutani, Phys. Rev. B **75**, 054109 (2007).
[38] J. C. Chervin, B. Canny, and M. Mancinelli, High Press. Res. **21**, 305 (2001).
[39] W. J. Moonan, J. Am. Stat. Assoc. **52**, 247 (1957).
[40] R. Y. Rubinstein and D. P. Kroese, *Simulation and the Monte Carlo Method*, 3rd ed. (John Wiley & Sons, Inc., New York, 2016).
[41] A.-L. Cholesky, Bull. Sabix **39**, 81 (2005).
[42] J. Sun, M. Martinez-Canales, D. D. Klug, C. J. Pickard, and R. J. Needs, Phys. Rev. Lett. **111**, 175502 (2013).
[43] R. Chau, A. C. Mitchell, R. W. Minich, and W. J. Nellis, Phys. Rev. Lett. **90**, 245501 (2003).
[44] P. M. Celliers, G. W. Collins, D. G. Hicks, and J. H. Eggert, J. Appl. Phys. **98**, 113529 (2005).
[45] H. K. Mao, J. Xu, and P. M. Bell, J. Geophys. Res. **91**, 4673 (1986).
[46] R. L. Mills, D. H. Liebenberg, and J. C. Bronson, J. Chem. Phys. **63**, 1198 (1975).
[47] D. Fabre and B. Oksengorn, Appl. Spectrosc. **46**, 468 (1992).
[48] H. D. Hochheimer, K. Weishaupt, and M. Takesada, J. Chem. Phys. **105**, 374 (1996).
[49] S. Jiang, N. Holtgrewe, S. S. Lobanov, F. Su, M. F. Mahmood, R. S. McWilliams, and A. F. Goncharov, Nat. Commun. **9**, 2624 (2018).
[50] S. Ninet, G. Weck, A. Dewaele, F. Datchi, V. M. Giordano, and P. Loubeyre, J. Chem. Phys. **153**, 114503 (2020).
[51] P. M. Celliers, D. K. Bradley, G. W. Collins, D. G. Hicks, T. R. Boehly, and W. J. Armstrong, Rev. Sci. Instrum. **75**, 4916 (2004).
[52] Y.-J. Kim, P. M. Celliers, J. H. Eggert, A. Lazicki, and M. Millot, Sci. Rep. **11**, 5610 (2021).
[53] D. G. Hicks, T. R. Boehly, P. M. Celliers, J. H. Eggert, S. J. Moon, D. D. Meyerhofer, and G. W. Collins, Phys. Rev. B **79**, 014112 (2009).
[54] S. Brygoo, M. Millot, P. Loubeyre, A. E. Lazicki, S. Hamel, T. Qi, P. M. Celliers, F. Coppari, J. H. Eggert, D. E. Fratanduono, D. G. Hicks, J. R. Rygg, R. F. Smith, D. C. Swift, G. W. Collins, and R. Jeanloz, J. Appl. Phys. **118**, 195901 (2015).
[55] M. P. Desjarlais, M. D. Knudson, and K. R. Cochrane, J. Appl. Phys. **122**, 035903 (2017).
[56] B. Militzer, F. González-Cataldo, S. Zhang, K. P. Driver, and F. Soubiran, Phys. Rev. E **103**, 013203 (2021).
[57] G. I. Kerley, arXiv:1306.6916v3.
[58] J. Eggert, S. Brygoo, P. Loubeyre, R. S. McWilliams, P. M. Celliers, D. G. Hicks, T. R. Boehly, R. Jeanloz, and G. W. Collins, Phys. Rev. Lett. **100**, 124503 (2008).
[59] R. F. Trunin, Phys. Usp. **44**, 371 (2001).
[60] H. B. Radousky, W. J. Nellis, M. Ross, D. C. Hamilton, and A. C. Mitchell, Phys. Rev. Lett. **57**, 2419 (1986).
[61] D. S. Moore, S. C. Schmidt, M. S. Shaw, and J. D. Johnson, J. Chem. Phys. **90**, 1368 (1989).
[62] Y. B. Zeldovich and Y. P. Raizer, *Physics of Shock Waves and High-Temperature Hydrodynamic Phenomena* (Elsevier, New York, 1967).
[63] B. Militzer, Phys. Rev. Lett. **97**, 175501 (2006).